Available online at www.sciencedirect.com
SCIENCE DIRECT
Journal of Power Sources 158 (2006) 354–360
JOURNAL OF POWER SOURCES
www.elsevier.com/locate/jpowsour

Oxidation kinetics and phase evolution of a Fe–16Cr alloy in simulated SOFC cathode atmosphere

Pu Jian [a], Li Jian [a,*], Hua Bing [a], Guangyuan Xie [b]

[a] *School of Materials Science and Engineering, State Key Laboratory of Plastic Forming Simulation and Die and Mould Technology, Huazhong University of Science and Technology, Wuhan, Hubei 430074, PR China*
[b] *School of Materials Science and Metallurgical Engineering, Wuhan University of Science and Technology, Wuhan, Hubei 430080, PR China*

Received 24 August 2005; accepted 21 September 2005
Available online 29 November 2005

Abstract

The oxidation behavior of a Fe–16Cr alloy containing a small amount of Mn oxidized in air for up to 500 h within the temperature range of 650–850 °C was examined. Two consecutive oxidation stages were found and these obeyed the parabolic rate law with various rate constants. Formation and growth of Cr_2O_3, $MnCr_2O_4$, surface nodules and oxide spallation were found to be responsible in the oxidation stages accordingly to various situations. The thin film X-ray diffraction, SEM and EDX confirmed the duplex oxide microstructure with $MnCr_2O_4$ on top of Cr_2O_3, Cr and Mn diffusion in Cr_2O_3 is considered to be responsible for the formation of each layer, respectively. The estimated area specific resistance (ASR) suggests the possibility of using this alloy as the interconnect material in reduced temperature SOFCs, however, surface modification to enhance its oxidation and spallation resistances is desired.

Keywords: Fe–16Cr alloy; Oxidation kinetics; Interconnect; SOFC; ASR

1. Introduction

Solid oxide fuel cells (SOFCs) are high-energy power generation systems, directly converting the chemical energy of fossil fuels into electricity without combustion and mechanical processes [1–3]. The interconnect is a critical component in a SOFC stack, which separates the cathodic and anodic gases and provides the electrical connection between the single cells [4,5]. Recent studies have demonstrated that the operation on temperature of SOFCs can be reduced from 1000 to below 800 °C with approximately similar power density in a planar design [6–8]. The lowered operating temperatures makes it possible to introduce metallic alloys as SOFC interconnect materials. Advantages such as easy fabrication, good electrical conductivity and low material cost are the main reasons for the metallic interconnect application; however, requirements for the coefficient of thermal expansion (CTE) and area-specific resistance (ASR) have presented difficulties for the selection of materials.

Several kinds of Cr_2O_3-forming alloys have been undergone extensive examination as candidates for the interconnect materials [9–12], in which Fe–Cr alloys with Cr content higher than 16 wt.% have showed the possibility use for the interconnect component. They have a CTE of 12×10^{-6}, close to that of the state-of-the-art electrolyte materials YSZ (yttria-stabilized zirconia) [13]. Under the SOFC oxidizing conditions, Cr is preferentially oxidized to form a dense and well-adherent Cr_2O_3 layer. Since the diffusivity of the metallic cations in Cr_2O_3 layer is low, the Fe–Cr alloys possess acceptably high temperature oxidation resistance [14–16]. The addition of few tenths of a percent of Mn to the Fe–Cr alloys would lead to the formation of spinel $MnCr_2O_4$ [14–17]. Duplex oxide scale with $MnCr_2O_4$ on top of the dense Cr_2O_3 was reported in Fe–Cr–Mn alloy oxidized at 900 °C in air [18]. It has also been reported that such duplex oxide scales have excellent electronic properties at the SOFC operating temperatures [19,20], and their oxidation kinetics obey the parabolic rate law [18,20,21].

The present work examines the oxidation kinetics and corresponding phase evolution of a commercial Fe–16Cr alloy oxidized in air (simulating the SOFC cathode atmosphere) from 650 to 850 °C, by using the thin film X-ray diffraction, scanning

* Corresponding author. Tel.: +86 27 87557694; fax: +86 27 87544307.
E-mail address: plumarrow@126.com (L. Jian).

0378-7753/$ – see front matter © 2005 Elsevier B.V. All rights reserved.
doi:10.1016/j.jpowsour.2005.09.056

electron microscope (SEM) and energy dissipation spectroscopy (EDS), verifying the applicability of the Fe–16Cr alloy for the SOFC interconnect component.

2. Experimental

The Fe–16Cr alloy was provided by Yuhang Stainless Steels Ltd., containing 82.12 wt.% Fe, 16.86 wt.% Cr, 0.26 wt.% Mn and trace amount of Si, Ni, Al, C, P and S. Coupon specimens with dimensions of 25 mm × 25 mm × 1 mm were cut by using a electron discharge machine. The surface of the samples was polished with SiC abrasive paper up to 1200-grit, and washed in an ultrasonic cleaner in distilled water and acetone.

The cleaned specimens were weighed, heated in a furnace to 650, 750 and 850 °C in air, respectively, and held for up to 500 h. The weight gain with time was obtained by weighing different samples every 100 h with a Sartorius BS 124S electronic balance (accuracy of 10^{-4} g). The oxidized samples were characterized by using a FEI Sirion 200 field emission scanning electron microscope (SEM) with energy dissipation spectrum (EDS) attachment, in terms of oxide thickness and composition. The samples for the cross-section examination were mounted in Buhler epoxide and polished by using a Buhler automatic polisher. Since the thickness of the oxide layer formed on the alloy surface is of the order of microns, a thin film X-ray diffraction technique was employed to identify the surface oxide. The angle between the incident beam and oxidized surface was fixed at 1.2°, while the detector rotated continuously along the goniometer to receive the diffraction signal. A PANalytical X'Pert PRO X-ray diffractometer was used for this purpose under the conditions of 40 mA and 40 kV; the scanning rate was 10° min^{-1}, and the 2θ angle ranged from 20° to 80°. In addition, X-ray diffraction in the regular mode was also conducted as needed.

3. Results

3.1. Weight gain

Figs. 1–3 show the weight gain of the samples as a function of the oxidation time in stagnant air ($P_{O_2} = 0.21$ atm) at 650, 750 and 850 °C, respectively. The curves were plotted as the (weight gain/area)^2 against the time, so that the oxidation kinetics can be explicitly presented. At all the three-oxidation temperatures, two linear relationships were obtained, suggesting two stages of oxidation and parabolic kinetics for each of them. The oxidation stage transfer occurred after 200 h of oxidation and it was delayed by decrease of the oxidation temperature. The slope of each straight line dictates the parabolic rate constant k_w in terms of the weight change, the value for each stage according to

$$\frac{\Delta W}{A} = k_w t \quad (1)$$

is listed in Table 1, where ΔW is the weight gain, A is the sample surface area and t is the oxidation time.

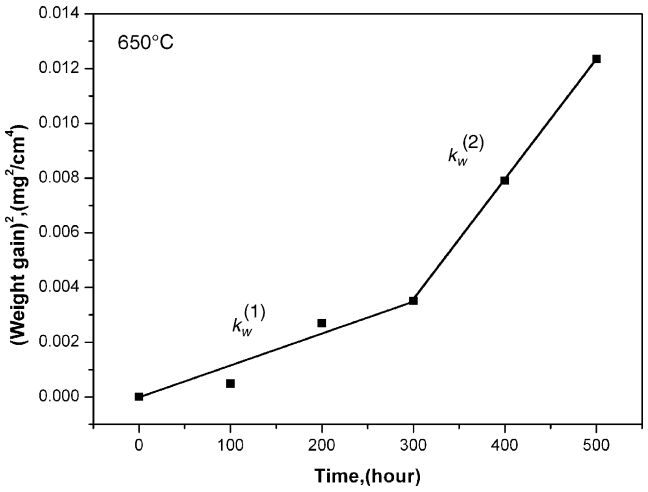

Fig. 1. Weight gain as a function of oxidation time for the Fe–16Cr alloy at 650 °C in air.

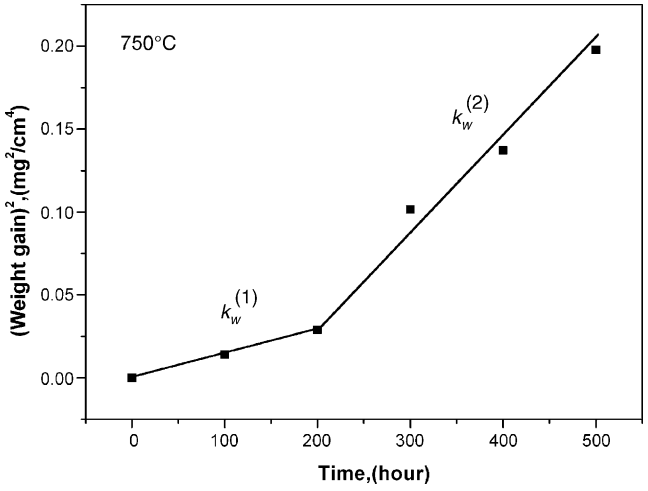

Fig. 2. Weight gain as a function of oxidation time for the Fe–16Cr alloy at 750 °C in air.

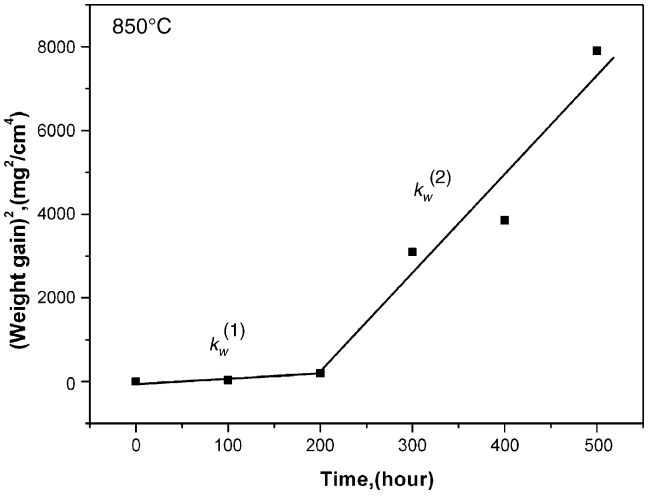

Fig. 3. Weight gain as a function of oxidation time for the Fe–16Cr alloy at 850 °C in air.

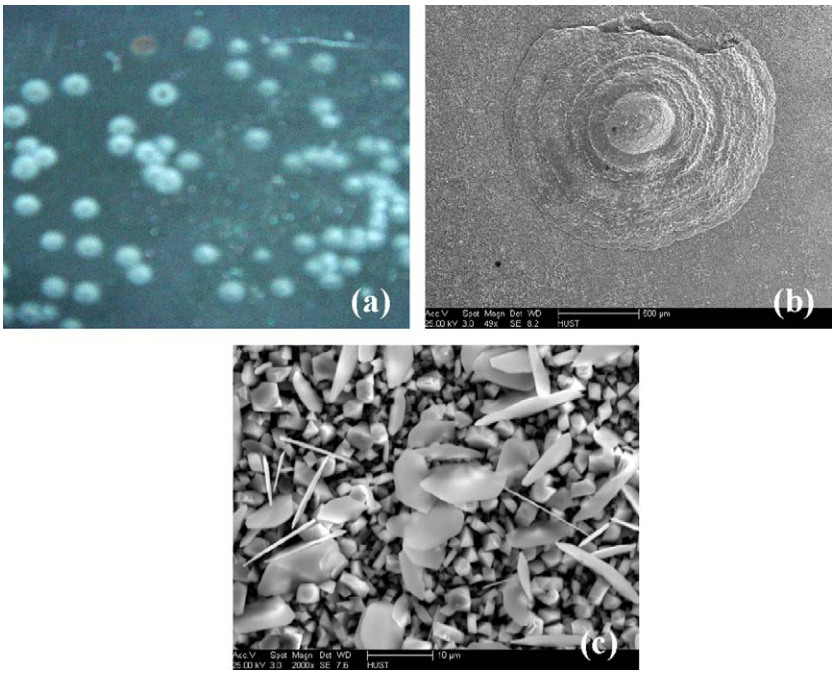

Fig. 4. Surface morphology of the Fe–16Cr alloy oxidized at 850 °C in air for 100 h: (a) macrograph of nodules formed on the surface, (b) high magnification image of the nodule and (c) microstructure of surface oxides.

3.2. Microstructure and composition of the oxide scale

Fig. 4 shows the surface morphology of the sample oxidized at 850 °C for 100 h. The surface was severely oxidized and nodules (Fig. 4a and b) were formed. In the area outside the nodules, the surface is decorated by flake- and prism-like oxides (Fig. 4c). According to the crystal structure of Cr_2O_3 (hcp) and $MnCr_2O_4$ (fcc), the flake shape oxide may be Cr_2O_3 and the prism-like oxide may be $MnCr_2O_4$. The nodules were the locations where the spallation of the oxide scale initiated. The structure inside the nodule is porous and flaky. With oxidation time prolonged, the nodules grew and coalesced to result in oxide scale spallation, as seen in Fig. 5, which shows the surface morphology of the sample oxidized at 850 °C for 300 h. For the samples oxidized at 650 and 750 °C in air for up to 500 h, spallation of oxide scales was not observed, even though a double layered oxide scale was formed, as seen in Fig. 6, which shows the cross-section SEM micrograph of the sample oxidized at 750 °C in air for 500 h. The corresponding EDS analysis suggests that the top thick layer is $MnCr_2O_4$ and the layer underneath is Cr_2O_3, the Mn intensity shown in Fig. 6c may be from the surrounding area due to the thickness of the Cr_2O_3 layer being less than the dimension of the so called tear-drop volume within which the EDS signals were collected.

Table 1
Parabolic rate constants ($g^2\,cm^{-4}\,s^{-1}$) for oxidation of the Fe–16Cr alloy at various temperatures

Parabolic rate constants	650 °C	750 °C	850 °C
$k_w^{(1)}$	3.54×10^{-15}	4.031×10^{-14}	2.82×10^{-10}
$k_w^{(2)}$	1.23×10^{-14}	1.54×10^{-13}	6.62×10^{-9}

Total oxidation time: 500 h.

3.3. Phases of the oxide scales

Fig. 7 shows the regular X-ray diffraction pattern from the sample oxidized at 850 °C in air for 100 h. The oxide scale contains significant amounts of spinel-type $MnCr_2O_4$ but less Cr_2O_3 phase. Due to the penetration of the X-ray beam into the depth of the sample, the signal generated from the substrate Fe–16Cr alloy were also collected as shown in Fig. 7. The Fe–16Cr alloy has a lack of high temperature strength at 850 °C; all the oxidized samples were warped, due to from their deadweight during the oxidation, and therefore, the thin-film X-ray diffraction was not conducted for this set of samples.

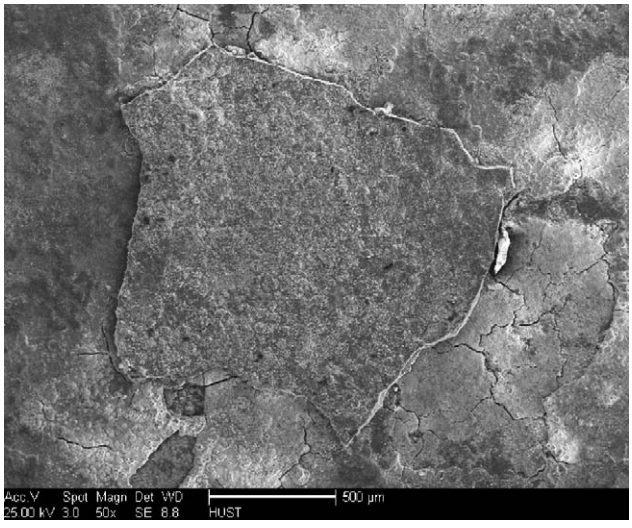

Fig. 5. Surface oxide spallation of the Fe–16Cr alloy oxidized at 850 °C in air for 300 h.

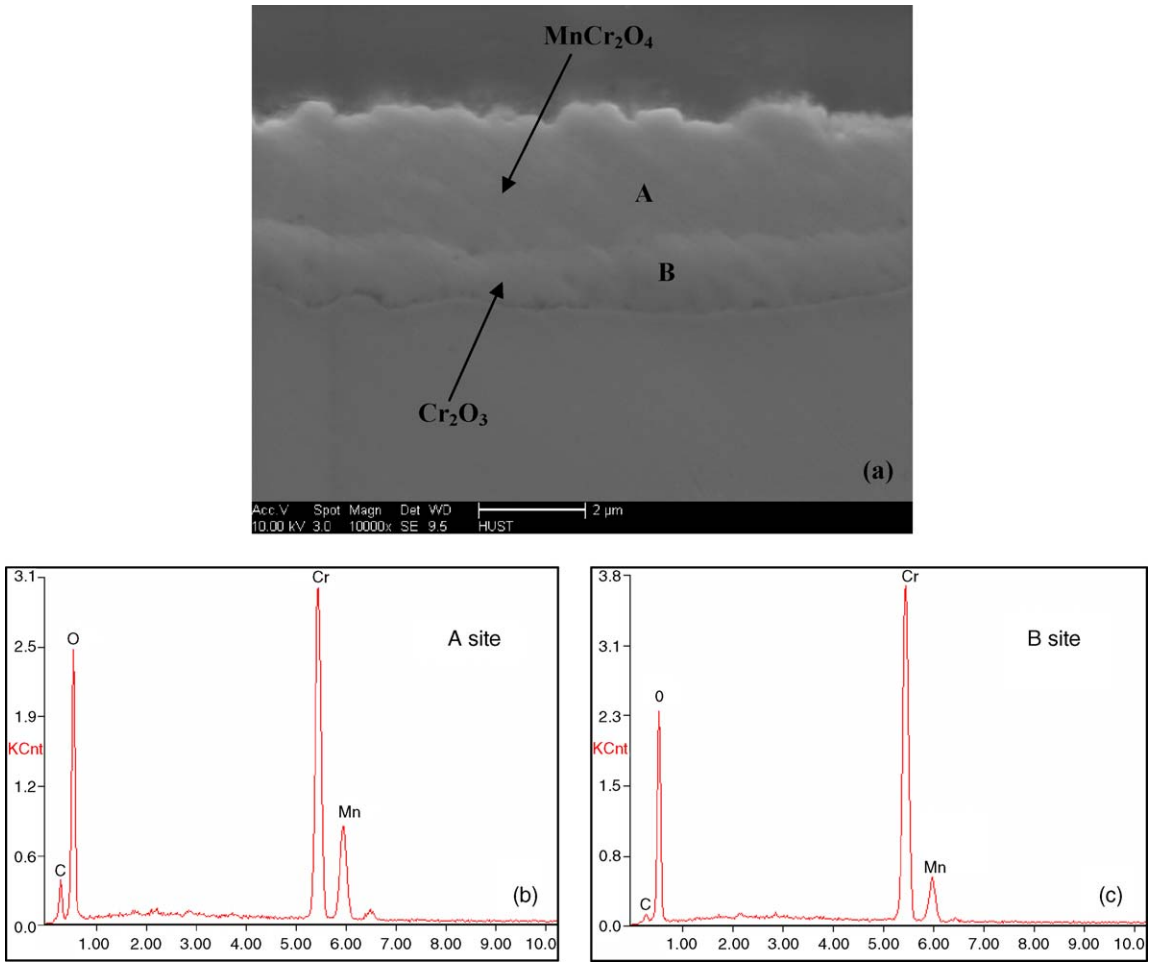

Fig. 6. SEM micrograph of the cross-section of the Fe–16Cr alloy at 750 °C in air for 500 h, showing duplex oxide scale with thickness around 2 (top) and 0.5 μm (below), respectively (a); EDS spectra taken from the A (b) and B (c) sites in (a).

Figs. 8 and 9 are the thin-film X-ray diffraction patterns for samples oxidized in air for up to 500 h at 650 and 750 °C, respectively. Cr_2O_3 and $MnCr_2O_4$ were identified without the signal originating from the substrate, which confirms the EDS analysis described above. At both 650 and 750 °C, the phase evolution shows a similar tendency that the intensity of $MnCr_2O_4$ gradually increases with oxidation time, and in the mean time the intensity from Cr_2O_3 is lowered, with the exception of the amount of Cr_2O_3 which increased in the sample oxidized at 650 °C for 500 h, while a trace amount of Mn_2O_3 was obtained. This result suggests a duplex oxide scale with a $MnCr_2O_4$ layer on top of Cr_2O_3 layer and possible decomposition of $MnCr_2O_4$ into Cr_2O_3 and Mn_2O_3 at 650 °C when the oxidation time is prolonged.

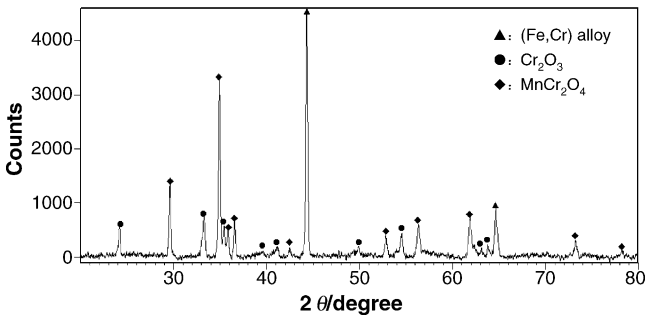

Fig. 7. X-ray diffraction pattern taken from the Fe–16Cr alloy oxidized at 850 °C in air for 100 h.

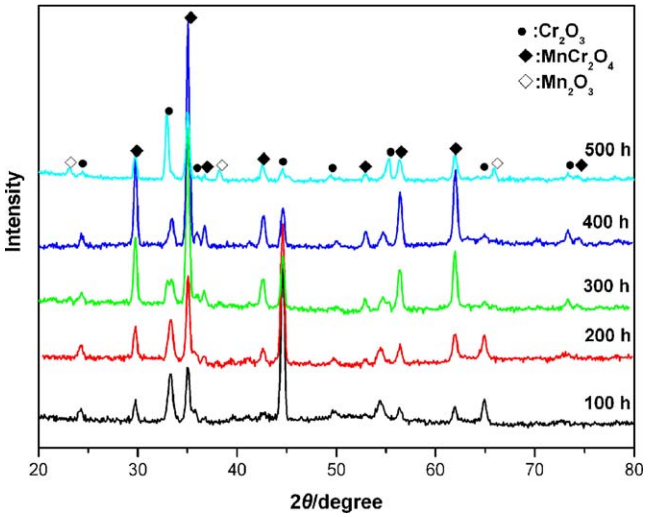

Fig. 8. Thin film X-ray diffraction patterns of the Fe–16Cr alloy oxidized at 650 °C in air for up to 500 h.

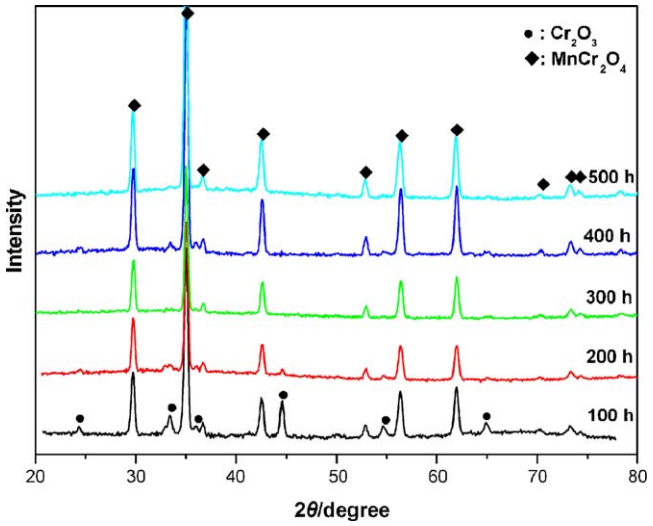

Fig. 9. Thin film X-ray diffraction patterns of the Fe–16Cr alloy oxidized at 750 °C in air for up to 500 h.

4. Discussion

4.1. Formation of various kinds of oxides

As mentioned above, the main reaction products in the oxide scale are Cr_2O_3 and spinel-type $MnCr_2O_4$ phases, which can be understood thermodynamically. Fig. 10 shows the standard Gibbs free energies of formation for Cr_2O_3 and MnO as a function of temperature. While exposed to air in the experimental temperature range, both Cr and Mn in the Fe–16Cr alloy are simultaneously oxidized to form Cr_2O_3 and MnO initially, and Cr_2O_3 and MnO may with react each other to form $MnCr_2O_4$ subsequently according to

$$Cr_2O_3 + MnO = MnCr_2O_4 \quad (2)$$

since

$$\Delta G^0_{MnCr_2O_4} = \Delta G^0_{Cr_2O_3} + \Delta G^0_{MnO} \quad (3)$$

that is more negative than either $\Delta G^0_{Cr_2O_3}$ or ΔG^0_{MnO} (as shown in Fig. 10); $MnCr_2O_4$ is thermodynamically more stable than both Cr_2O_3 and MnO. This explains that a few tenths of a percent of Mn lead to the formation of $MnCr_2O_4$ phase, when added to a binary Fe–Cr alloy [22].

In the present alloy, the content of Mn is around 0.26 wt.% which is much lower than that of the Cr 16.86 wt.%. A part of Cr_2O_3 participated in the reaction (3) to form $MnCr_2O_4$, and significant amount of Cr_2O_3 remained as a dense layer well adhering to the substrate as shown in Fig. 6. The thickness of the inner Cr_2O_3 phase and the outer $MnCr_2O_4$ phase increases progressively with oxidation time, so that the X-ray diffraction intensity generated from the inner Cr_2O_3 is gradually lowered (see Figs. 8 and 9) due to the shallow penetration of the small angled incident X-ray beam. Fig. 11 schematically demonstrates the proposed oxide scale formation procedures. Comparing Figs. 8 and 9, a thinner outer $MnCr_2O_4$ layer formed on samples oxidized at 650 °C is suggested, which is consistent with the lower k_w at the same temperature (see Table 1).

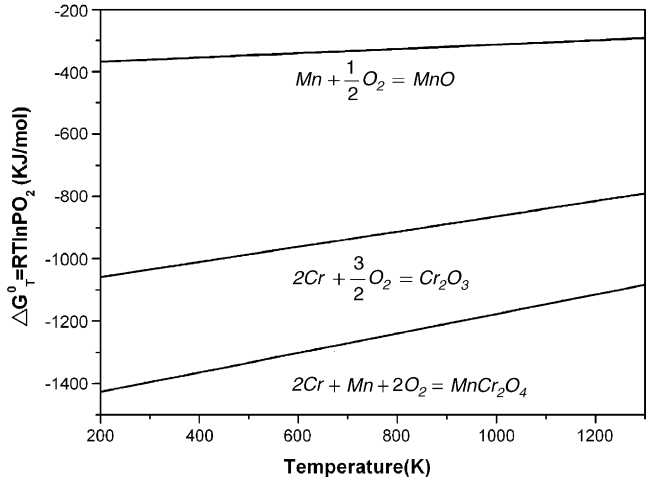

Fig. 10. Dependence of standard Gibbs free energy of formation of oxides on temperature for Cr_2O_3, MnO and $MnCr_2O_4$ phases.

4.2. Oxidation kinetics

The present Fe–16Cr alloy exhibited two-stage oxidation kinetics at the various temperatures studied, represented by $k_w^{(1)}$ and $k_w^{(2)}$. This first stage oxidation has a lower parabolic rate constant $k_w^{(1)}$ than that of the second state oxidation $k_w^{(2)}$. The relation between the oxidation rate constant k_w and temperature could be described by the Arrhenius equation:

$$k_w = k_{w0} \exp\left(-\frac{Q}{RT}\right) \quad (4)$$

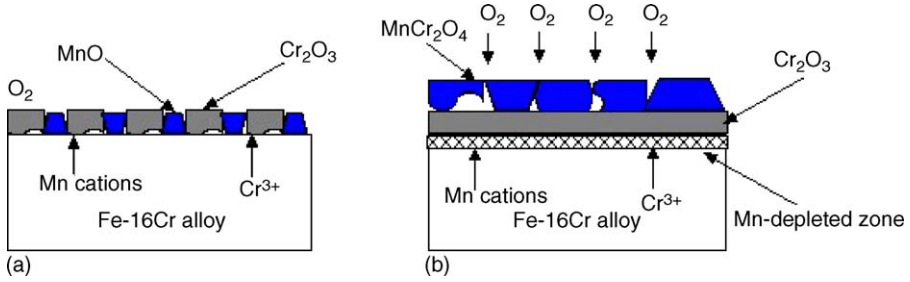

Fig. 11. Schematic illustration of oxidation processes of the Fe–16Cr alloy in air.

Table 2
Activation energies (Q) and pre-exponential constants k_{w0} for oxidation of the Fe–16Cr alloy in comparison with previous studies

Materials	Q (kJ mol^{-1})	k_{w0} (g^2 cm^{-4} s^{-1})	Temperature range (°C)	Reference
Fe–16Cr ($k_w^{(1)}$)	192.8	2.48×10^{-4}	650–750	Present work
Fe–16Cr ($k_w^{(2)}$)	198.4	1.74×10^{-3}	650–750	Present work
Pure Cr	247	0.11	700–1200	[23]
Fe–16Cr	202.3	6.8×10^{-4}	750–900	[15]

Where k_{w0} is the pre-exponential factor, Q the activation energy, R the gas constant and T is the absolute temperature. Fig. 12 shows the k_w dependence on temperature with the data from the literature [15,23] presented. The activation energies and pre-exponential factors for both stages are calculated in the temperature range between 650 and 750 °C (see Table 2). The activation energies for both stages are similar even though the rate constants are different, and consistent with that for Cr and cation diffusion in Cr_2O_3, suggesting an outward diffusion of cations to form the oxide scale. For the oxidation at 850 °C, the rate constants for both stages are much greater than those for oxidation at 650 and 750 °C, a different oxidation mechanism may be implied.

Two-stage oxidation was reported in Fe–Cr–Mn alloys [18], which was explained by the formation of M_3O_4 type oxide preceded by the growth of M_2O_3 type oxide. The growth rate of M_3O_4 was considered an order of magnitude greater than that of the growth of an M_2O_3 layer. As reported by Caplan et al. [24], in Fe–Cr–Mn alloys, the Mn rapidly diffuse from the alloy to the surface to form a Mn-rich oxide scale, causing severe local Mn depletion until the alloy Mn flux was re-established. The underlying alloy adjacent to the Mn-rich oxide scale has a transient composition approximating to the Fe–Cr alloy, resulting in formation of Cr_2O_3. According to Wagner's parabolic oxidation theory, the oxidation rate of the alloy is governed by the diffusion of cations passing a dense oxide scale. In the present study, the first stage oxidation at 650 and 750 °C can be considered to correspond to the formation and growth of Cr_2O_3 subsequent to the initial formation of Mn-enriched $MnCr_2O_4$. Owing to the sluggish diffusion of Cr ions in the Cr_2O_3 scale [25], the oxidation rate is relatively slow. The second stage oxidation may correspond to the growth of $MnCr_2O_4$ after the re-establishment of Mn flux. The content of Mn in the present alloy is quite low; the re-establishment may take a longer time than that in the higher Mn content alloys. The time needed for Mn flux re-establishment is also temperature dependant, and a longer time is required at the lower oxidation temperature as indicated in Fig. 3. $MnCr_2O_4$ forms at the gas–scale interface, and thickens as a result of Mn diffusion through Cr_2O_3. As is known, Mn ion diffusion is an order of magnitude faster than Cr ion in Cr_2O_3 [26–28], resulting in a rapider oxidation rate in the second stage.

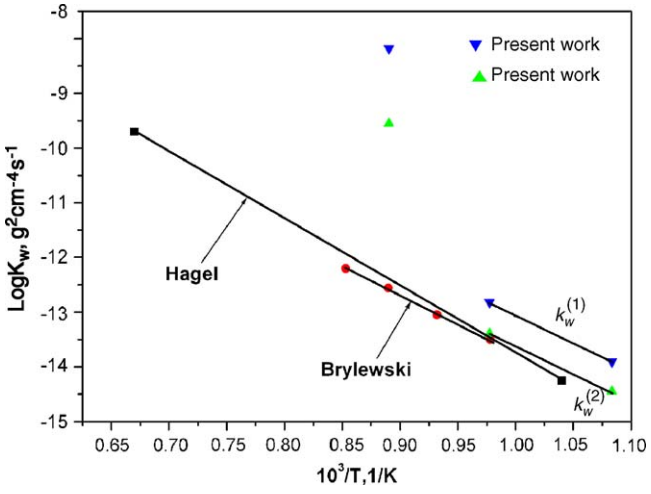

Fig. 12. A comparison of the parabolic rate constants, k_w, of the Fe–16Cr alloy with those reported in previous studies.

At 850 °C, the oxidation kinetics is several orders of magnitude higher than that at 650 and 750 °C for both stages. From Figs. 4 and 7, it can be seen that within first 100 h of oxidation, significant amounts of Cr_2O_3, $MnCr_2O_4$ and surface nodules were formed. Nodule growth and coalescence caused the scale spallation at 300 h of oxidation (see Fig. 5). The formation of nodules in oxidation was also reported in higher Mn-content Fe–Cr–Mn alloys previously [18]. It is considered that the formation is associated with the breakdown of the protective Cr_2O_3 layer. With Cr_2O_3 layer thickening, the mismatch of the coefficient of thermal expansion between Cr_2O_3 and the substrate alloy, always thermal stress to build at the interface, leading to local cracks in the Cr_2O_3 layer. Consequently, fast local outward diffusion of cations is favored to form the nodules. The first stage of oxidation can be recognized as the combination of Cr_2O_3, $MnCr_2O_4$ and nodule formation. The second stage is expected to be corresponded to the nodule coalescence and scale spallation.

4.3. Estimation of area specific resistance (ASR)

For SOFC interconnect application, the ASR is required to be smaller than 0.1 Ω cm^2 after 40,000 h of operation at 750 °C, the typical operating temperature for the reduced temperature SOFCs. In order to evaluate the applicability of the Fe–16Cr alloy, an estimation of the ASR value is necessary.

Cross section observation (Fig. 6) revealed that a duplex oxide scale with total thickness of 2.5 μm formed after oxidation at 750 °C for 500 h. The thickness of the inner and the outer oxide layers was about 0.5 and 2 μm, respectively. The relation between the thickness of the oxide scale Δt and weight gain ΔW can be described as

$$\Delta t = \frac{\Delta W}{d} \quad (5)$$

where d is the density of oxide. For the current duplex oxide scale, the ASR may be expressed as

$$\mathrm{ASR} = \rho_{Cr_2O_3}\Delta t_{Cr_2O_3} + \rho_{MnCr_2O_4}\Delta t_{MnCr_2O_4} \quad (6)$$

where $\rho_{Cr_2O_3}$ and $\rho_{MnCr_2O_4}$ are the electrical resistivity of Cr_2O_3 and $MnCr_2O_4$, respectively. Taking the parabolic rate constants listed in Table 1 for 750 °C and the densities of C_2O_3 5.1 g cm^{-3} and $MnCr_2O_4$ 4.94 g cm^{-3}, the extrapolated $\Delta t_{Cr_2O_3}$ and $\Delta t_{MnCr_2O_4}$ for 40,000 h are 4.72 and 9.53 μm, respectively. However, the Mn content in this alloy is limited. Assuming all of the Mn in the alloy is used to form $MnCr_2O_4$ phase and the Cr_2O_3 grows with the same rate thereafter, the estimated ASR would be 0.0373 Ω cm^2 for both sides of oxidation, while taking the literature reported electrical resistivity of Cr_2O_3 and $MnCr_2O_4$ as ∼78 [29] and ∼0.5 Ω cm [30], respectively. This value is less than the conventionally acceptable value 0.1 Ω cm^2 of the ASR. Therefore, it may be able to say that the Fe–16Cr alloy is suitable for the interconnect application in a SOFC operated at 750 °C for 40,000 h. However, considering the temperature fluctuations in the SOFC stack, the poor oxidation resistance at temperature higher than 750 °C, for example 850 °C, and the tendency of oxide spallation, surface modification of the Fe–16Cr alloy to increase its oxidation resistance and spallation resistance is required before the application.

5. Conclusions

The Fe–16Cr alloy demonstrated two-stage oxidation kinetics when oxidized at 650, 750 and 850 °C in air for up to 500 h, each obeyed the parabolic rate law. At 650 and 750 °C, the first stage oxidation corresponded to the growth of Cr_2O_3 layer, and the faster second stage oxidation corresponded to the growth of $MnCr_2O_4$ due to the rapider diffusion of Mn ions than Cr in Cr_2O_3. In the case of 850 °C, the slower first stage was a combination of formation of Cr_2O_3, $MnCr_2O_4$ and surface nodules; local breakdown of Cr_2O_3 layer was the possible mechanism for the nodule formation, and the second stage represented the nodule coalescence and oxide scale spallation. A duplex oxide scale was observed with $MnCr_2O_4$ layer on top of Cr_2O_3 layer which is well adhered to the substrate. Thin film X-ray diffraction and composition analysis confirmed the observation. Activation calculations suggested outward diffusion of Cr and Mn ions to form the oxide scale. The estimated ASR value with assumptions indicated that the Fe–16Cr alloy might be considered for the reduced temperature SOFC interconnect applications, however, surface modification to increase its oxidation resistance and oxide spallation resistance is desirable.

Acknowledgements

This research was financially supported by the National Science Foundation of China under the project contract 50471063, the "863" high-tech project under contract 204AA32G070. The authors would like to thank Prof. Sun Daqian of Materials Characterization Center of Huazhong University of Science and Technology for his assistance in X-ray diffraction and Sr. Engineer Xu Mingying of School of Materials Science and Engineering of Huazhong University of Science and Technology for metallographic sample preparation.

References

[1] P. Singh, N.Q. Minh, Int. J. Appl. Ceram. Technol. 1 (2004) 5–15.
[2] S.C. Singhal, Solid State Ionics 152–153 (2003) 405–410.
[3] Fuel Cell Handbook, 5th ed., EG&G Services, National Technical Information Service, U.S. Department of Commerce, 2000.
[4] W.Z. Zhu, S.C. Deevi, Mater. Sci. Eng. A348 (2003) 227–243.
[5] I. Yasuda, M. Hishimuma, J. Electrochem. Soc. 143 (1996) 1583.
[6] S. de Souza, S.J. Visco, L.C. De Jonghe, J. Electrochem. Soc. 144 (1997) L35.
[7] K.Q. Hung, R. Tichy, J.B. Goudenough, J. Am. Ceram. Soc. 81 (1998) 2565.
[8] Y.J. Leng, S.H. Chan, K.A. Khor, Int. J. Hydrogen Energy 29 (2004) 1025–1033.
[9] T. Brylewski, J. Dabek, K. Przybylski, J. Therm. Anal. Calorim. 77 (2004) 207–216.
[10] W.A. Meulenberg, S. Uhlenbruck, E. Wssel, J. Mater. Sci. 38 (2003) 507–513.
[11] W.Z. Zhu, S.C. Deevi, Mater. Res. Bull. 38 (2003) 957–972.
[12] K.Q. Huang, P.Y. Hou, J.B. Goodenough, Solid State Ionics 129 (2000) 237–250.
[13] Fuel cell Handbook, The U.S. Department of energy, 2002.
[14] T. Horita, Y.P. Xiong, K. Yamaji, J. Power Sources 118 (2003) 35–43.
[15] T. Brylewski, M. Nanko, T. Maruyama, Solid State Ionics 143 (2001) 131–150.
[16] H. Kurokawa, K. Kawamura, T. Maruyama, Solid State Ionics 168 (2004) 13–21.
[17] S.K. Yen, Y.C. Tsai, J. Electrochem. Soc. 143 (1996) 2493.
[18] A.L. Marasco, D.J. Young, Oxid. Met. 36 (1991) 157.
[19] F.F. Fava, I. Baraille, A. Lichanot, J. Phys: Condens. Matter 9 (1997) 10715.
[20] Qu Wei, Master Thesis, University of Calgary, Canada, 2004.
[21] T. Horita, Y.P. Xiong, K. Yamaji, J. Electrochem. Soc. 150 (2003) A243.
[22] I.J. Yearian, E.C. Randell, T.A. Longo, Corrosion 12 (1956) 55.
[23] W.C. Hagel, Trans. Am. Soc. Met. 56 (1963) 583.
[24] D. Caplan, P.E. Beaubien, M. Cohen, Trans. AIME 233 (1965) 766.
[25] R.E. Lobnig, H.P. Schmidt, K. Hennesen, Oxid. Met. 27 (1992) 81.
[26] R.K. Wild, Corrsion Sci. 17 (1977) 87.
[27] M.G.E. Cox, B. Mcenanay, V.D. Scott, Phila. Mag. 26 (1972) 839.
[28] D. Caplan, P.E. Beaubien, M. Cohen, Trans. AIME 233 (1965) 766.
[29] G.V. Samsonov, The Oxide Handbook, translated from Russian by C. Nigel Turton and T. Turton, IFI/Plenum, 1973.
[30] A.V. Virkar, U.S. Patent 6,054,231 (April 25, 2000).